Solar system chaos and the Paleocene-Eocene boundary age constrained by geology and astronomy

Richard E. Zeebe[1,*] and Lucas J. Lourens[2]

*Corresponding Author.

[1]School of Ocean and Earth Science and Technology, University of Hawaii at Manoa, 1000 Pope Road, MSB 629, Honolulu, HI 96822, USA. zeebe@soest.hawaii.edu

[2]Department of Earth Sciences, Faculty of Geosciences, Utrecht University, Princetonlaan 8a, 3584 CB Utrecht, The Netherlands. L.J.Lourens@uu.nl

July 30, 2019

Science, accepted.

Astronomical calculations reveal the solar system's dynamical evolution, including its chaoticity, and represent the backbone of cyclostratigraphy and astrochronology. An absolute, fully calibrated astronomical time scale has hitherto been hampered beyond ∼50 Ma, because orbital calculations disagree before that age. Here we present geologic data and a new astronomical solution (ZB18a), showing exceptional agreement from ∼58 to 53 Ma. We provide a new absolute astrochronology up to 58 Ma and a new Paleocene-Eocene boundary age (56.01±0.05 Ma). We show that the Paleocene-Eocene Thermal Maximum (PETM) onset occurred near a 405-kyr eccentricity maximum, suggesting an orbital trigger. We also provide an independent PETM duration (170±30 kyr) from onset to recovery inflection. Our astronomical solution requires a chaotic resonance transition at ∼50 Ma in the solar system's fundamental frequencies.

Numerical solutions [†] for the solar system's orbital motion provide Earth's orbital parameters in the past, widely used to date geologic records and investigate Earth's paleoclimate (1–11). The solar system's chaoticity imposes an apparently firm limit of ~50 Ma on identifying a unique orbital solution, as small differences in initial conditions/parameters cause astronomical solutions to diverge around that age (Lyapunov time ~5 Myr, see Supplementary Materials) (4, 6, 12, 13). Recent evidence for a chaotic resonance transition (change in resonance pattern, see below) in the Cretaceous (Libsack record) (9) confirms the solar system's chaoticity but, unfortunately, does not provide constraints to identify a unique astronomical solution. The unconstrained interval between the Libsack record (90-83 Ma) and 50 Ma is too large a gap, allowing chaos to drive the solutions apart (see Supplementary Materials). Thus, proper geologic data around 60-50 Ma is essential to select a specific astronomical solution and, conversely, the astronomical solution is essential to extend the astronomically calibrated time scale beyond 50 Ma.

We analyzed color reflectance data (a^*, red-to-green spectrum) (7, 8) at Ocean Drilling Program (ODP) Site 1262 (see Supplementary Materials); a^*-1262 for short, a proxy for changes in lithology (7). The related Fe-intensity proxy (8)

[†] Solutions for Earth's orbital eccentricity and inclination are available at `www2.hawaii.edu/~zeebe/Astro.html` and `www.ncdc.noaa.gov/paleo/study/26970`. We provide results from 100-0 Ma but caution that the interval 100-58 Ma is unconstrained due to chaos.

gives nearly identical results (Fig. S4). We focus on the section ∼170-110 m (∼58-53 Ma), which exhibits a remarkable expression of eccentricity cycles at Site 1262 (refs. 7, 8, 10, 14, 15), less so in the preceding (older) section. Our focus interval includes the PETM and Eocene Thermal Maximum 2 (ETM2), extreme global warming events (hyperthermals), considered the best paleo-analogs for the climate response to anthropogenic carbon release (16–18). The PETM's trigger mechanism and duration remains highly debated (19–21). Thus, in addition to geological and astronomical implications, unraveling the chronology of events in our studied interval is critical for understanding Earth's past and future climate.

We developed a simple floating chronology, attempting to use a minimum number of assumptions (see Supplementary Materials). We initially employed a uniform sedimentation rate throughout the section (except for the PETM) and a root mean square deviation (RMSD) optimization routine to derive ages (for final age model and difference from previous work, see Supplementary Materials). No additional tuning, wiggle-matching, or pre-existing age model was applied to the data. Using our floating chronology, the best fit between the filtered and normalized data target a^{**} (a-double-star, Fig. 1) and a given astronomical solution was obtained through minimizing the RMSD between record and solution by shifting a^{**} along the time axis (offset τ) over a time interval of ±200 kyr, with ETM2 centered around 54 Ma (see Supplementary Materials). Before applying the minimization, both a^{**} and the solution were demeaned, linearly detrended, and normalized to their respective standard deviation (Fig. 1).

It turned out that one additional step was necessary for a meaningful comparison between a^{**} and astronomical solutions. Relative to all solutions tested here, a^{**} was consistently offset (shifted towards the PETM after optimizing τ) by ∼one short eccentricity cycle for ages either younger (some solutions) or older than the PETM (other solutions). The consistent offset relative to the PETM suggests that the condensed PETM interval in the data record is the culprit, for which we applied a correction, also obtained through optimization. At Site 1262, the PETM is marked by a ∼16 cm clay layer (<1-wt% $CaCO_3$), largely due to dissolution and some erosion across the interval (16, 22), although erosion of Paleocene (pre-PETM) sediment alone can not account for the offset of ∼one short eccentricity cycle (see Supplementary Materials). Sedimentation rates were hence nonuniform across the PETM interval (8, 10, 16) and primary lithologic cycles from variations in $CaCO_3$ content are not preserved within the clay layer. Thus, we corrected the condensed interval by stretching a total of k grid points across the PETM by Δz for a total length of $\Delta L = k\Delta z$ and included k as a second parameter in our optimization routine (see Fig. 1). Essentially, the correction for the reduction/gap in carbonate sedimentation across the PETM is determined by the entire record, except the PETM itself (see Supplementary Materials). In summary, we minimized the RMSD between data target and solution by a stretch-shift operation, i.e., we simultaneously optimized the number of stretched PETM grid points (k) and the overall time shift (τ) between floating chronology and solution.

Our new astronomical solution ZB18a (computations build on our earlier work (6, 23, 24), see Supplementary Materials) agrees exceptionally well with the final a^{**} record (Fig. 1b) and has the lowest RMSD of all 18 solutions published to date that cover the interval (Table 1). The 18 solutions were computed by multiple investigators, representing different solution classes due to initial conditions, parameters, etc. (see Sections S6, S7). Based on ZB18a, we provide a new astronomically calibrated age model to 58 Ma (see Fig. 1b and Supplementary Materials) and a revised age for the P/E boundary (PEB) of 56.01 ± 0.05 Ma (see Supplementary Materials for errors). Our PEB age differs from previous ages (8, 25–27) but is close to approximate estimates from 405-kyr cycle counting across the Paleocene (28) (see Supplementary Materials).

Contrary to current thinking (8, 14, 20, 27, 29), the PETM onset therefore occurred temporally near, not distant, to a 405-kyr maximum in Earth's orbital eccentricity (Fig. 1, cf. also ref. 10). As for ETM2 and successive early Eocene hyperthermals (7, 29, 30), this suggests an orbital trigger for the PETM, given theoretical grounding and extensive, robust observational evidence for eccentricity controls on Earth's climate (2, 7–10, 14, 20, 26–32). Note, however, that the onset does not necessarily coincide with a 100-kyr eccentricity maximum (see below). Our analysis also provides an independent PETM main phase duration of 170±30 kyr from onset to recovery inflection (for tie points, see Fig. S6 and Supplementary Materials). This duration might be an underestimate, given that sedimentation rates increased during the PETM recovery (compacting the recovery would require additional stretching of the main phase). Our duration is significantly longer than 94 kyr (ref. 20) but agrees with the ^{3}He age model at Site 1266 ($167\pm^{34}_{24}$ kyr) (21) and is consistent with >8 cycles in Si/Fe ratios at Zumaia (31), which, we suggest, are full (not half) precession cycles.

If high orbital eccentricity (e) also contributed to the long PETM duration ($e \simeq 0.025 - 0.044$ during PETM), then the potential for prolonged future warming from eccentricity is reduced due to its currently low values ($e \simeq 0.0024 - 0.0167$ during next 100 kyr). A similar argument may hold for eccentricity-related PETM trigger mechanisms. The PETM occurred superimposed on a long-term, multimillion year, warming trend (7, 30). Our solution ZB18a shows a 405-kyr eccentricity maximum around the PETM but reduced 100-kyr variability (Fig. 1b). Eccentricity in ZB18a remained high prior to the PETM for one short eccentricity cycle (Fig. 1b, arrow), suggesting the combination of orbital configuration and background warming (30, 32) forced the Earth system across a threshold, resulting in the PETM. While similar thresholds may exist in the modern Earth system, the current orbital configuration (lower e) and background climate (Quaternary/Holocene) are different from 56 million years ago. None of the above, however, will directly mitigate future warming and is therefore no reason to downplay anthropogenic carbon emissions and climate change.

Our astronomical solution ZB18a shows a chaotic resonance transition (change in resonance pattern) (33) at ∼50 Ma, visualized by wavelet analysis (34) of the classical variables:

$$h = e \ \sin \varpi \qquad ; \qquad p = \sin(I/2) \ \sin \Omega \, , \tag{1}$$

where e, I, ϖ, and Ω are eccentricity, inclination, longitude of perihelion, and longitude of ascending node of Earth's orbit, respectively (Fig. 2). The wavelet spectrum highlights several fundamental frequencies (g's and s's) of the solar system, corresponding to eigenmodes. For example, g_3 and g_4 are loosely related to the perihelion precession of Earth's and Mars' orbits (s_3 and s_4 correspondingly to the nodes). The g's and s's are constant in quasiperiodic systems but vary over time in chaotic systems (see Supplementary Materials). Importantly, the period P_{43} associated with $g_4 - g_3$ switches from ∼1.5 Myr to ∼2.4 Myr in ZB18a at ∼50 Ma, characteristic of a resonance transition (see arrow, Fig. 2) (33). Remarkably, an independent analysis of the a^*-1262 record recently also reconstructed $P_{43} \simeq 1.5$ Myr (35) within the interval ∼56-54 Ma. However, our individual g-values from ZB18a are different from the reconstructed mean values, although within their 2σ error bounds (see Supplementary Materials).

Notably, parameters required for long-term integrations compatible with geologic observations (e.g., ZB18a vs. a^{**}, Fig. 1) appear somewhat incompatible with our best knowledge of the current solar system. For instance, ZB18a is part of a solution class featuring specific combinations of number of asteroids and solar quadrupole moment (J_2), with J_2 values lower than recent evidence suggests (Supplementary Materials). In addition, the La10c solution (33) with a small RMSD (see Table 1) used the INPOP08 ephemeris, considered less accurate than the more recent INPOP10 used for La11 (13). Yet, La10c fits the geologic data better than La11 (Table 1 and ref. (27)).

The resonance transition in ZB18a is an unmistakable manifestation of chaos and also key to distinguishing between different solutions before ~50 Ma, e.g., using the $g_4 - g_3$ term. This term modulates the amplitude of eccentricity and, e.g., the interval between consecutive minima in a 2-Myr filter of eccentricity (Fig. 3). Other solutions such as La10c (33) also show a resonance transition around 50 Ma. However, the pattern for ZB18a is different prior to 55 Ma, which is critical for its better fit with the data record from 58-53 Ma (smaller RMSD, see Table 1, Fig. 1). For example, $P_{43} \simeq 2$ and ~1.6 Myr at ~59 and ~56 Ma in La10c but is rather stable at ~1.5-1.6 Myr across this interval in ZB18a. Briefly, to explain the geologic record, our astronomical solution requires that the solar system is (a) chaotic and (b) underwent a specific resonance transition pattern between ~60-50 Myr BP.

References and Notes

1. H. Poincaré, *Les méthodes nouvelles de la mécanique céleste, Vol. 1* (Gauthier-Villars, Paris, 1892).
2. M. Milanković, *Kanon der Erdbestrahlung und seine Anwendung auf das Eiszeitproblem* (Königl. Serb. Akad., Belgrad, pp. 633, 1941).
3. J. D. Hays, J. Imbrie, N. J. Shackleton, *Science* **194**, 1121 (1976).
4. F. Varadi, B. Runnegar, M. Ghil, *Astrophys. J.* **592**, 620 (2003).
5. J. Laskar, *et al.*, *Astron. Astrophys.* **428**, 261 (2004).
6. R. E. Zeebe, *Astron. J.* **154**, 193 (2017).
7. L. J. Lourens, *et al.*, *Nature* **435**, 1083 (2005).
8. T. Westerhold, *et al.*, *Paleoceanogr.* **22**, 2201 (2007).
9. C. Ma, S. R. Meyers, B. B. Sageman, *Nature* **542**, 468 (2017).
10. M. Li, L. R. Kump, L. A. Hinnov, M. E. Mann, *Earth Planet. Sci. Lett.* **501**, 165 (2018).
11. C. Spalding, W. W. Fischer, G. Laughlin, *Astrophys. J.* **869**, L19 (2018).
12. A. Morbidelli, *Modern Celestial Mechanics: Aspects of Solar System Dynamics* (Taylor & Francis, London, 2002).
13. J. Laskar, M. Gastineau, J.-B. Delisle, A. Farrés, A. Fienga, *Astron. Astrophys.* **532**, L4 (2011).
14. S. R. Meyers, *Paleoceanogr.* **30**, 1625 (2015).
15. S. R. Meyers, *Earth-Sci. Rev.* **190**, 190 (2019).
16. Zachos, J. C., U. Röhl, S. A. Schellenberg, A. Sluijs, D. A. Hodell, D. C. Kelly, E. Thomas, M. Nicolo, I. Raffi, L. J. Lourens, H. McCarren, and D. Kroon, *Science* **308**, 1611 (2005).
17. IPCC, Intergovernmental Panel on Climate Change, Stocker, T. F. et al. (Eds.), *Climate Change 2013: The Physical Science Basis* (Cambridge University Press, Cambridge, pp. 1535, 2013).
18. R. E. Zeebe, A. Ridgwell, J. Z. Zachos, *Nature Geosci.* **9**, 325 (2016).
19. F. A. McInerney, S. L. Wing, *Ann. Rev. Earth Planet. Sci.* **39**, 489 (2011).
20. Röhl, U., T. Westerhold, T. J. Bralower, and J. C. Zachos, *Geochem. Geophys. Geosyst.* **8**, Q12002, doi:10.1029/2007GC001784 (2007).
21. B. H. Murphy, K. A. Farley, J. C. Zachos, *Geochim. Cosmochim. Acta* **74**, 5098 (2010).
22. Zeebe, R. E. and J. C. Zachos, *Paleoceanogr.* **22**, PA3201, doi:10.1029/2006PA001395 (2007).
23. R. E. Zeebe, *Astrophys. J.* **798**, 8 (2015a).

24. R. E. Zeebe, *Astrophys. J.* **811**, 9 (2015b).

25. C. Jaramillo, *et al.*, *Science* **330**, 957 (2010).

26. A. J. Charles, *et al.*, *Geochem. Geophys. Geosys.* **12**, Q0AA17, doi:10.1029/2010GC003426 (2011).

27. T. Westerhold, *et al.*, *Clim. Past* **13**, 1129 (2017).

28. F. J. Hilgen, K. F. Kuiper, L. J. Lourens, *Earth Planet. Sci. Lett.* **300**, 139 (2010).

29. B. S. Cramer, J. D. Wright, D. V. Kent, M.-P. Aubry, *Paleoceanogr.* **18**, 1097 (2003).

30. J. C. Zachos, H. McCarren, B. Murphy, U. Röhl, T. Westerhold, *Earth Planet. Sci. Lett.* **299**, 242 (2010).

31. T. Dunkley Jones, *et al.*, *Clim. Past* **14**, 1035 (2018).

32. R. E. Zeebe, T. Westerhold, K. Littler, J. C. Zachos, *Paleoceanogr.* **32**, 1 (2017).

33. J. Laskar, A. Fienga, M. Gastineau, H. Manche, *Astron. Astrophys.* **532**, A89 (2011).

34. M. Ghil, *et al.*, *Rev. Geophys.* **40**, 3 (2002).

35. S. R. Meyers, A. Malinverno, *Proceedings of the National Academy of Science* **115**, 6363 (2018).

36. J. C. Zachos, D. Kroon, P. e. a. Blum, *Proc. ODP, Init. Repts.* **208**, 1 (2004).

37. V. Lauretano, J. C. Zachos, L. J. Lourens, *Paleoceanogr. Paleoclim.* **33**, 1050 (2018).

38. T. Westerhold, U. Röhl, B. Donner, J. C. Zachos, *Paleoceanogr. Paleoclim.* **33**, 626 (2018).

39. K. P. Rauch, D. P. Hamilton, *AAS/Division of Dynamical Astronomy Meeting #33* (2002), vol. 34 of *Bull. Am. Astron. Soc.*, p. 938.

40. J. Wisdom, M. Holman, *Astron. J.* **102**, 1528 (1991).

41. T. R. Quinn, S. Tremaine, M. Duncan, *Astron. J.* **101**, 2287 (1991).

42. W. M. Folkner, J. G. Williams, D. H. Boggs, R. S. Park, P. Kuchynka, *Interplanetary Network Progress Report* **196**, 1 (2014).

43. J. Laskar, *Nature* **338**, 237 (1989).

44. C. Ma, S. R. Meyers, B. B. Sageman, *Earth Planet. Sci. Lett.* **513**, 1 (2019).

45. F. P. Pijpers, *Mon. Not. R. Astron. Soc.* **297**, L76 (1998).

46. R. Mecheri, T. Abdelatif, A. Irbah, J. Provost, G. Berthomieu, *Sol. Phys.* **222**, 191 (2004).

47. A. Fienga, J. Laskar, P. Exertier, H. Manche, M. Gastineau, *Celest. Mech. Dyn. Astron.* **123**, 325 (2015).

48. E. V. Pitjeva, N. P. Pitjev, *Celest. Mech. Dyn. Astron.* **119**, 237 (2014).

49. R. S. Park, *et al.*, *Astron. J* **153**, 121 (2017).

50. J. Lense, H. Thirring, *Physikalische Zeitschrift* **19** (1918).

51. M. H. Soffel, *Relativity in Astrometry, Celestial Mechanics and Geodesy* (Springer-Verlag Heidelberg, pp. 208, 1989).

52. L. Iorio, *Astron. Astrophys.* **431**, 385 (2005).

53. A. Fienga, *et al.*, *Astron. Astrophys.* **507**, 1675 (2009).

54. A. Fienga, *et al.*, *Celest. Mech. Dyn. Astron.* **111**, 363 (2011).

55. T. Westerhold, U. Röhl, J. Laskar, *Geochem. Geophys. Geosys.* **13**, Q06015 (2012).

56. J. Laskar, *Icarus* **88**, 266 (1990).

57. G. J. Sussman, J. Wisdom, *Science* **257**, 56 (1992).

58. T. Westerhold, *et al.*, *Palaeogeogr. Palaeoclim. Palaeoecol.* **257**, 377 (2008).

59. V. Lauretano, F. Hilgen, J. Zachos, L. Lourens, *Newsletters on Stratigraphy* **49**, 383 (2016).

Acknowledgments. Funding: REZ acknowledges support from the US National Science Foundation (OCE16-58023). This research was supported by the Netherlands Organisation for Scientific Research (NWO-ALW 865.10.001) and by the Netherlands Earth System Science Centre (NESSC 024.002.001) to LJL. We are grateful to the International Ocean Discovery Program for drilling and exploring ODP Site 1262. **Author contributions:** REZ and LJL devised the study and wrote the manuscript. LJL was instrumental in guiding the cyclostratigraphic analyses and selecting the a*-1262 record. REZ led the numerical integrations for the orbital motion of the solar system. **Competing interests:** The authors declare no competing interests. **Data and materials availability:** Solutions for Earth's orbital eccentricity and inclination are available at `www2.hawaii.edu/~zeebe/Astro.html` and `www.ncdc.noaa.gov/paleo/study/26970`. We provide results from 100-0 Ma but caution that the interval 100-58 Ma is unconstrained due to chaos.

The Supplementary Materials include:

Materials and Methods
Supplementary Text
Figs. S1 to S8
Tables S1 to S3
References 36-59

Table 1. RMSD[a] between a^{**} record and selected astronomical solutions.[b]

Solution	ZB18a[c,d]	ZB17a	ZB17b	La10c	La10a	La11	Va03
RMSD	0.6820	0.9108	1.0358	0.7431	0.9854	1.0009	0.9611

[a] Root mean square deviation.

[b] Record and solution were demeaned, detrended, and normalized to their standard deviation before calculating RMSD.

[c] Z and B in ZB18a derive from **Z**eebe-HN**B**ody (6).

[d] Lowest RMSD of 18 solutions published to date: ZB17a-k ($N = 11$) (6), La10a-d (4) (33), La11 (1) (13), La04 (1) (5), Va03 (1) (4) (7/18 listed).

Figure 1. Data analysis and comparison of color reflectance a^* to our astronomical solution ZB18a. (a) a^* at ODP Site 1262 (blue-green), interpolated, demeaned, detrended record (Norm. a^*) including PETM stretch (light-blue); scaled long/short eccentricity cycle filter (blue/gray), PETM onset (up-triangle), PETM recovery inflection (down-triangle), Elmo (square); mcd = meters composite depth. As primary $CaCO_3$ variations within the PETM interval are not preserved due to dissolution and erosion, the interval was cropped. (b) Sum of long and short cycle filter outputs in the time domain (data target a^{**}, light blue) and normalized eccentricity of Earth's orbit from our astronomical solution ZB18a (purple). a^{**} and ZB18a were demeaned, detrended, and normalized to their respective standard deviation before optimization (RMSD minimization between a^{**} and solution by stretch-shift operation, see text). Across the cropped PETM interval, a^{**} provides no actual information and is omitted. Up-triangle and error bar indicate our new age for the P/E boundary (PEB/PETM onset) of 56.01 ± 0.05 Ma. Arrow: prolonged high eccentricity period prior to PETM (see text).

Figure 2. Wavelet analysis of astronomical solution. Wavelet analysis (34) of (a) $h = e\ \sin\varpi$ and (b) $p = \sin(I/2)\sin\Omega$ from our astronomical solution ZB18a (see text). g's and s's indicate fundamental frequencies of the solar system's eigenmodes (multiple frequencies are expressed in the spectrum of a single planet). For example, g_3 and g_4 are loosely related to the perihelion precession of Earth's and Mars' orbits. The wavelet amplitude (red = peaks, blue = valleys) in, e.g., the g_3 and g_4 frequency band is modulated by the period $1/(g_4 - g_3) \simeq$ 2.4 Myr for ages younger ∼45 Ma, where $g_3 \simeq 1/74.61$ kyr^{-1} and $g_4 \simeq 1/72.33$ kyr^{-1} (ref. 6). Correspondingly, $1/(s_4 - s_3) \simeq$ 1.2 Myr. However, in our solution, the period associated with $g_4 - g_3$ switches from ∼1.5 Myr to ∼2.4 Myr across the resonance transition around 50 Ma (arrow). The ratio $(g_4 - g_3) : (s_4 - s_3) \simeq$ 1:2 after ∼45 Ma and closer to 1:1 before but appears irregular.

Figure 3. Resonance transition in selected astronomical solutions. Interval between consecutive minima (Δt_{min}) in 2-Myr Gaussian filter (±60%) of Earth's orbital eccentricity for selected solutions (6, 33). The rise of Δt_{min} around 50 Ma in ZB18a and La10c indicate resonance transitions. However, note distinct pattern of ZB18a before 55 Ma. Hence our solution ZB18a (closest agreement with the data record, see Fig. 1) requires that the solar system underwent a specific chaotic resonance transition pattern between ∼60-50 Myr BP.

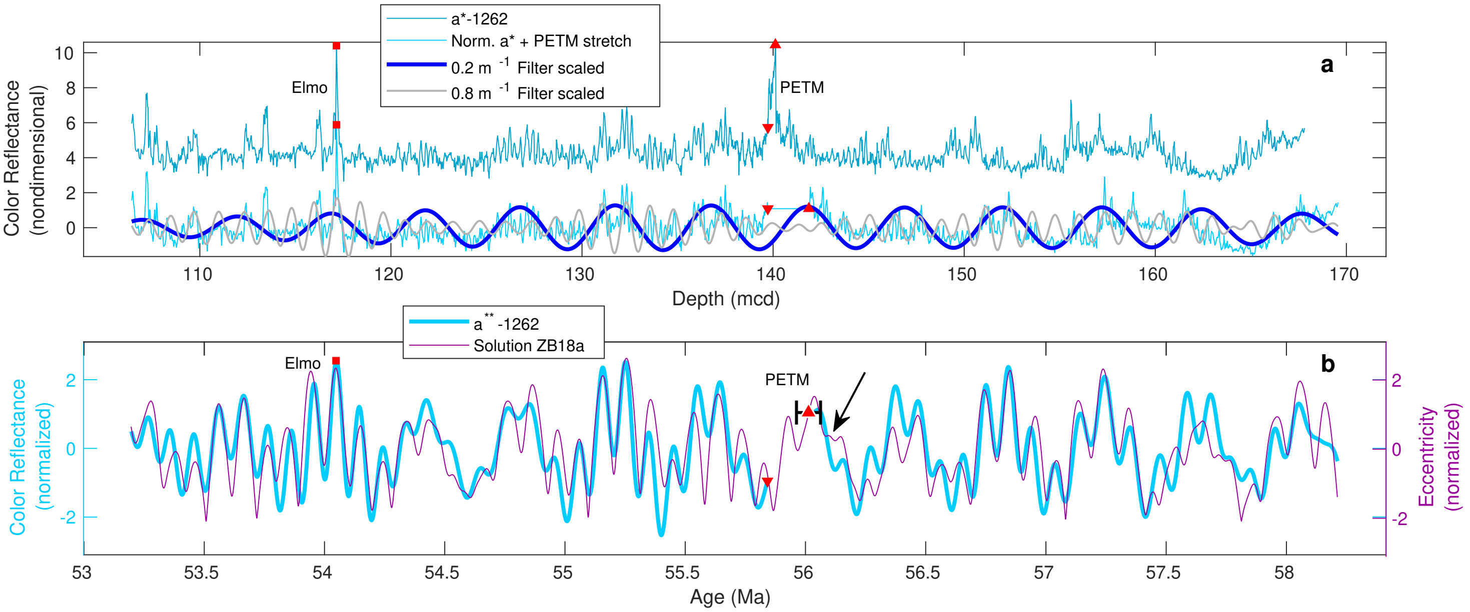
a*-1262
Norm. a* + PETM stretch
0.2 m -1 Filter scaled
0.8 m -1 Filter scaled
a
Elmo
PETM
Color Reflectance (nondimensional)
10
8
6
4
2
0
110
120
130
140
150
160
170
Depth (mcd)
a** -1262
Solution ZB18a
b
Elmo
PETM
Color Reflectance (normalized)
Eccentricity (normalized)
2
0
-2
53
53.5
54
54.5
55
55.5
56
56.5
57
57.5
58
Age (Ma)

Figure 1.

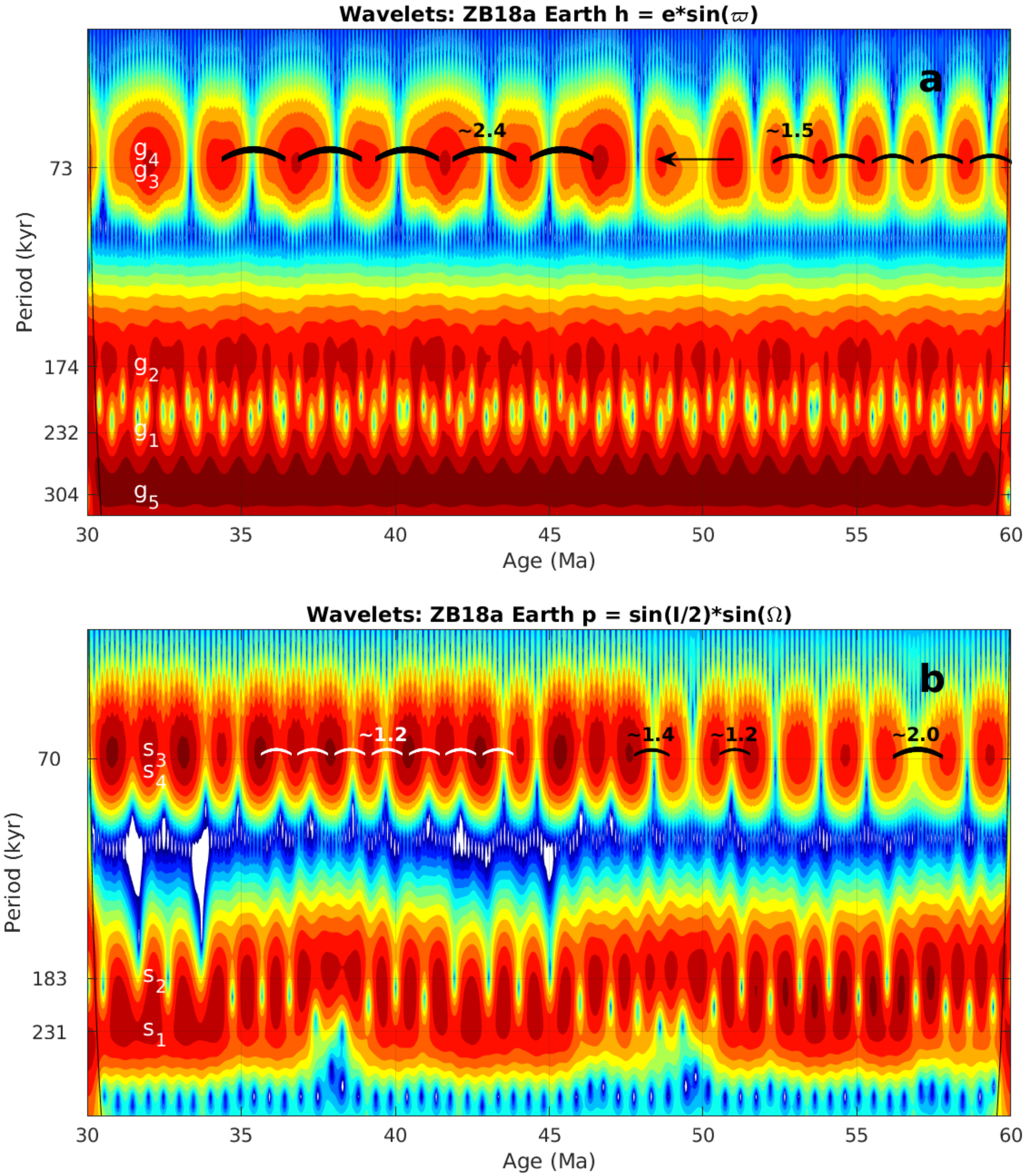
Wavelets: ZB18a Earth h = e*sin(ϖ)
a
~2.4
~1.5
g4
g3
g2
g1
g5
73
174
232
304
Period (kyr)
30
35
40
45
50
55
60
Age (Ma)
Wavelets: ZB18a Earth p = sin(I/2)*sin(Ω)
b
~1.2
~1.4
~1.2
~2.0
s3
s4
s2
s1
70
183
231
Period (kyr)
30
35
40
45
50
55
60
Age (Ma)

Figure 2.

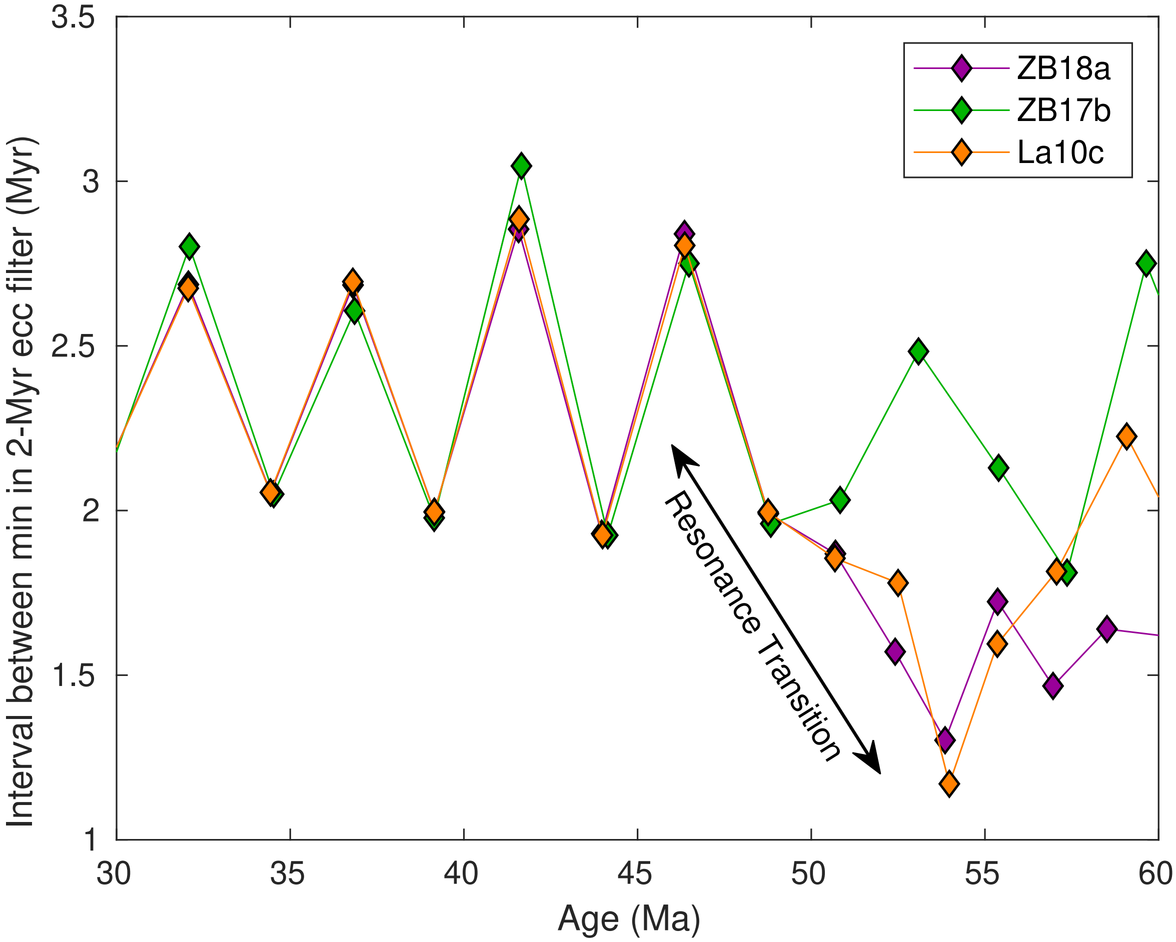
3.5
3
2.5
2
1.5
1
30
35
40
45
50
55
60
Interval between min in 2-Myr ecc filter (Myr)
Age (Ma)
ZB18a
ZB17b
La10c
Resonance Transition

Figure 3.